Magnetically driven phase transitions with a large volume collapse in MnSe under pressure: A DFT+DMFT study

Alexey A. Dyachenko,[1,*] Alexey V. Lukoyanov,[1,2] Alexey O. Shorikov,[1,2] and Vladimir I. Anisimov[1,2]
[1]*M.N. Miheev Institute of Metal Physics of Ural Branch of Russian Academy of Sciences, 620990 Yekaterinburg, Russia*
[2]*Ural Federal University, 620002 Yekaterinburg, Russia*

(Received 17 April 2018; revised manuscript received 28 June 2018; published 23 August 2018)

We present a theoretical study of spectral, magnetic, and structural properties of the manganese selenide under pressure within the DFT+DMFT method combining density functional theory with dynamical mean-field theory. Our results reveal that a high-spin to low-spin transition occurs upon compression at volumes below 33 Å^3. The spin-state transition is accompanied by a metal-insulator transition and a structural phase transition with the large volume collapse of ∼20% from the cubic B1 structure to the high-pressure MnP-type B31 structure at about 27 Å^3. We find that the spin-state transition is the main driving force for the structural transition.

DOI: 10.1103/PhysRevB.98.085139

I. INTRODUCTION

Pressure-driven phase transitions have attracted a lot of interest in recent years. Despite considerable amount of investigations dedicated to comprehend this phenomenon, some difficulties in its understanding still arise due to complex interplay of various mechanisms. An important example of such interplay is a pressure-driven structural transition in chalcogenides, which is accompanied by a change of spin state from high-spin (HS) to low-spin (LS) [1–4]. Nowadays theoretical DFT+DMFT method (density functional theory with dynamical mean field theory) [5] is a unique and powerful technique to explore material properties and structural, metal-insulator, and spin transitions under pressure [6–12]. Understanding of mechanisms of these transitions is crucial for the evaluation of the state of Earth's interior [13].

Manganese chalcogenides MnS and MnSe exhibit large cell-volume collapse during pressure-induced phase transitions [3,4]. Both Mn compounds crystallize in a rock-salt NaCl-type B1 ($Pm\bar{3}m$) structure at normal conditions, unlike MnTe, which crystallizes in a NiAs-type B8 hexagonal structure [14]. However, at temperatures below 300 K MnSe undergoes structural and magnetic transformations, which make studies of its properties complicated; there are two phase transitions: Below 155 K a part of the sample transforms to the magnetically ordered NiAs-type structure, which persists up to 300 K, then below 122 K the remains of the B1 structure become magnetic (long range antiferromagnetic order with AFM direction [111] [15]). Complex structural and magnetic transformations at lower temperatures lead to a large diversity of reported values of the Néel temperature, which varies from 122 to 249 K [16–18]. Both MnS and MnSe undergo the phase transition from cubic NaCl-type to orthorhombic MnP-type B31 ($Pnma$) with the large volume collapse of about 22% in the region of 20–30 GPa with an unknown tetrahedral phase in between [3,4]. The phase transition was found to be coupled with the Mn^{2+} high-spin $S = 5/2$ to low-spin $S = 1/2$ state transition and the formation of Mn-Mn intermetallic bonds. The metallization at 25 GPa was also shown by the measurements of electrical resistance [4].

A number of experimental and theoretical works have been carried out so far to understand the electronic structure of MnSe. Experimental studies of the valence-band and conduction-band densities of states of MnSe by the means of photoemission spectroscopy (PES) and inverse-photoemission spectroscopy (IPES) performed by Sato *et al.* [19] show that a spin exchange splitting energy is $U_{\text{eff}} = 7.4$ eV, a band gap is 2.0 eV, and found that Mn-3d states have localized character. Several main features were found in the partial Mn-3d density of states (DOS): valence bands positioned from 0 to −2.5 eV, the main peak is positioned at −3.5 eV, which is attributed to the localized states with t_2 symmetry, and a multielectron satellite structure is at −8.0 eV. Additionally, the experimental spectra were analyzed within configuration interaction theory using Coulomb interaction parameter $U = 4$ eV, which provides the best fit. The electronic structure of MnSe was also considered within density functional theory. In an earlier work by Youn *et al.* [20] MnSe was investigated within local density approximation with accounting for Coulomb interaction (LDA+U method [21]). In that work the direct Coulomb and exchange Hund interaction parameters were calculated to be $U = 6.1$ eV and $J_H = 0.86$ eV, respectively. As a result, they found the conduction-band and valence-band minima to be a mix between Mn-3d and Se-4p bands and concluded that the MnSe is between band and charge transfer insulators. Similar results were obtained by Amiri *et al.* [22] within generalized gradient approximation with Coulomb interaction (GGA+U method). They used the value of Coulomb interaction parameter $U = 2.0$ eV, which resulted in exchange splitting energy similar to the experimentally reported value. Furthermore, they found the band gap to be 1.30 eV and reported that further increase of U parameter has no effect on the band gap. In agreement with previous LDA+U work, they found the band gap is formed by the Mn-3d and Se-4p states. Magnetically ordered state with [111] moment direction was simulated in

*dyachenko@imp.uran.ru

both works. Also, DFT+U gave sizable improvement with respect to the results of GGA or LDA calculations of magnetic moment which was found $\sim$4.6 μ_B.

Existing theoretical and experimental studies of the pressure-driven transition in manganese chalcogenides suggest that the high- to low-spin transition is the driving force of the structural transitions under pressure [3,4,7]. Spin and metal-insulator transitions in compounds with strong correlations in 3d shell have been successfully studied by means of the DFT+DMFT method combining density functional theory with dynamical mean-field theory [5]. This method describes correctly magnetic state and reproduces spin, metal-insulator, and structural transitions under pressure due to accounting for dynamic effects and strong electronic correlations in many transition metal compounds, e.g., MnO [7], (Mg,Fe)O [8], $FeBO_3$ [10], $BiFeO_3$ [11], CoO [23], Fe_2O_3 [24], $FeSiO_3$ [25], and FeS [26].

In the present paper we employ the DFT+DMFT approach to investigate the electronic structure and magnetic properties of the manganese selenide MnSe and its structural stability under high pressure. We found that MnSe undergoes a structural transition from the cubic B1 to MnP-type B31 structure with a $\sim$20% cell-volume collapse and the pressure-induced spin transition of Mn^{2+} ions is its main reason. Moreover the spin transition is accompanied by the insulator-to-metal transition.

II. METHOD

The computational scheme of DFT+DMFT method [5] starts from self-consistent DFT calculations, using plane-wave pseudopotentials [27] with generalized gradient approximation implemented in QUANTUM-ESPRESSO package [28], producing a noninteracting Hamiltonian, then a many-body Hamiltonian is set up, and finally the DMFT equations for this Hamiltonian are solved self-consistently. For the Mn-3d, Mn-4s, Mn-4p, Se-4s, and Se-4p orbitals, we constructed a basis set of Wannier functions [29,30] employing the projection procedure described in detail in Ref. [31]; all bands of the basis set formed by the chosen states were included and projected on Bloch functions for these bands.

All calculations were performed at electronic temperature of 1000 K ($\beta = 11.6\ \mathrm{eV}^{-1}$), well above the Néel temperature to ensure paramagnetic state. The orthorhombic MnP-type B31 structure was relaxed within GGA calculations with a variable-cell relaxation method [32] as implemented in QUANTUM-ESPRESSO. We performed several relaxation runs, using various magnetic orders within DFT and DFT+U methods, and found that nonmagnetic noncorrelated GGA calculation results in the lowest total energy.

The interaction matrix for the quantum impurity model was parameterized by values of Coulomb repulsion parameter U and Hund exchange parameter J_H in the density-density approximation. Interaction parameters were calculated by the constrained-DFT method [21] on Wannier functions [31]; Coulomb repulsion parameter was found to vary slightly with structure and pressure and was chosen as average $U = 6.0$ eV to simplify the total energy fitting, and J_H was found to be invariant of pressure and chosen to be 0.8 eV (influence of J_H value on magnetic properties and HS to LS transition is discussed below). We used fully localized limit form for double counting correction. The continuous time quantum Monte Carlo hybridization-expansion solver from the AMULET package [33] was employed to solve effective DMFT quantum impurity problem [34]. Some codes from the ALPS Project were used for the calculations [35]. Presented spectral functions were calculated from the real frequency lattice Green functions $G(\omega)$ using the Páde approximant [36] for analytical continuation to the real energy axis, as implemented in the AMULET package.

Calculations of the total energy in the DFT+DMFT method were performed as follows:

$$E = E_{\mathrm{total}}^{\mathrm{DFT}} + E_{\mathrm{kin}}^{\mathrm{DMFT}} - E_{\mathrm{kin}}^{\mathrm{DFT}} - E_{\mathrm{DC}}^{\mathrm{DMFT}} + E_{\mathrm{Coulomb}}^{\mathrm{DMFT}}, \quad (1)$$

where $E_{\mathrm{total}}^{\mathrm{DFT}}$ is the total energy of noninteracting problem, $E_{\mathrm{kin}}^{\mathrm{DMFT}}$ and $E_{\mathrm{kin}}^{\mathrm{DFT}}$ are the DMFT and DFT kinetic energy, $E_{\mathrm{DC}}^{\mathrm{DMFT}}$ and $E_{\mathrm{Coulomb}}^{\mathrm{DMFT}}$ are double-counting correction and Coulomb correlation contributions to the total energy, respectively; the details of total energy calculation in the DFT+DMFT method can be found elsewhere [37]. The obtained total energy curves were fit with the Rose-Vinet equation of state [38]. We note that obtained curves were also fit with the Burch-Murnaghan equation of state [39] and the results were very similar; the Rose-Vinet equation of state was used as it behaves better with high compression ratios and with statistically noisy data, e.g., the DFT+DMFT results.

III. RESULTS AND DISCUSSION

We started with a structural optimization of the reported experimental high-pressure MnP-type B31 structure of MnSe using the variable-cell relaxation method. Resulting lengths of Mn-Mn intermetallic bonds in the optimized structure at the volume which corresponds to experimental 30 GPa are 2.70 Å and 2.76 Å (reported experimental values [4] are 2.65 Å and 2.85 Å). We obtained the parameters of the equation of state by fitting total energy from the DFT calculations: equilibrium volume $V_0 = 30.03(27.70)$ Å^3 and bulk modulus $B_0 = 132(160)$ GPa for the B1 (B31) structure. Here and further we use volume per Mn atom. The obtained GGA values differ considerably from reported previously $V_0 = 40$ Å^3 and $B_0 = 68$ GPa for the B1 structure and $B_0 = 218$ GPa for the B31 structure [4,40,41] and from the results of magnetic GGA+U for the B1 structure ($V_0 = 41.14$ Å^3 and $B_0 = 61.6$ GPa) [22]. The optimized MnP-type structure has lower DFT total energy than the B1 structure at all investigated volumes with the equilibrium energy E_0 difference of -1.02 eV; this is similar to the previous report on MnS where GGA calculations revealed the MnP-type phase to have lower energy at 10 GPa and above [3].

In Fig. 1(a), we present the values of local magnetic moment $\sqrt{\langle \mu_z^2 \rangle}$ computed within the DFT+DMFT method for both structures at different volumes. One can see that at ambient pressure (AP) both structures are in the HS state with the value of a local magnetic moment $\sqrt{\langle \mu_z^2 \rangle}$ of $\sim$4.75 μ_B, in good agreement with the experimental value of magnetic moment 4.45 μ_B and the theoretical estimate 4.6 μ_B [22]. With the increase of pressure, the HS-LS transition is observed and the value of local magnetic moment $\sqrt{\langle \mu_z^2 \rangle}$ drops to $\sim$1.6 μ_B at

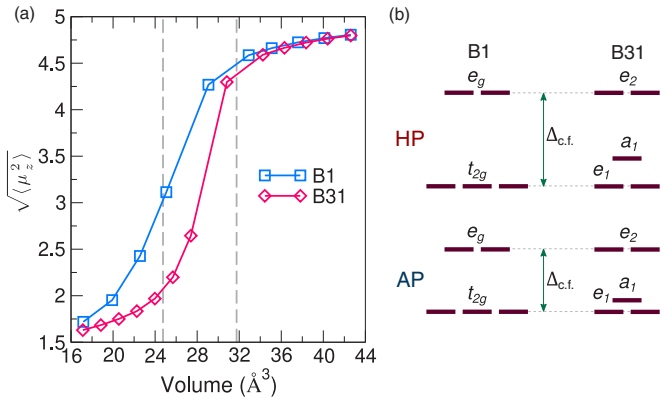

FIG. 1. (a) Local magnetic moment $\sqrt{\langle\mu_z^2\rangle}$ of Mn-3d the manganese selenide MnSe calculated by the DFT+DMFT method at 1000 K for the cubic B1 and MnP-type B31 structures. The experimental phase transition volume range is shown by vertical dashed lines. (b) Schematic representation of crystal field splitting of Mn-3d in both structures at ambient and high pressures.

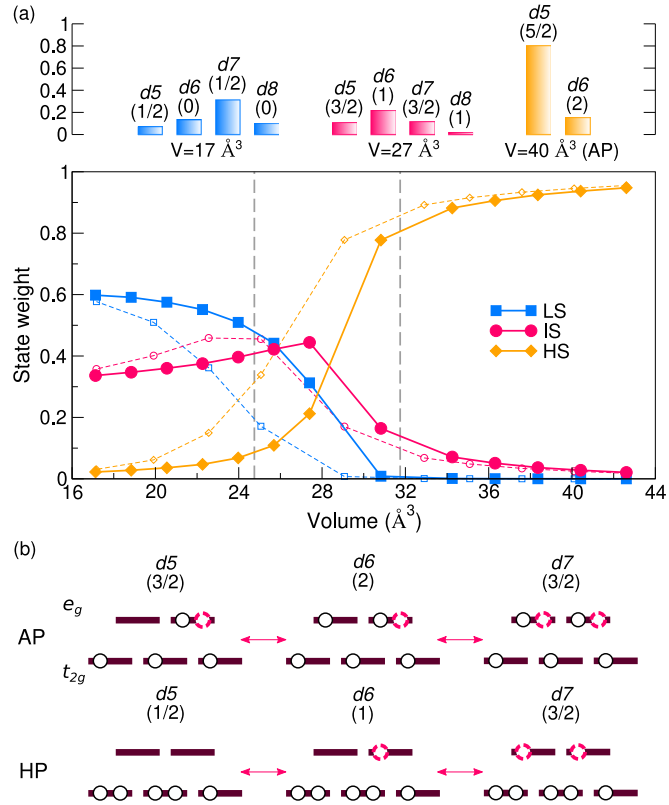

FIG. 2. (a) Calculated within the DFT+DMFT method cumulative weights of the high-, low-, and intermediate-spin electronic configurations of the Mn-3d quantum impurities versus volume for the cubic B1 (dashed lines) and B31 (solid lines) structures. At the top: calculated configuration content of each spin state at its respective maximum (see details in text). (b) Some of the high probability electronic configurations and possible bath-impurity hybridization events as an example of formation of the intermediate-spin configurations. Electrons associated with hybridization are shown as red circles.

17 Å^3. The calculated values of local magnetic moment $\sqrt{\langle\mu_z^2\rangle}$ indicate that the spin crossover begins at ∼30 Å^3 for both structures. The B31 structure reaches saturation of the LS state much earlier at ∼20–24 Å^3. In contrast, the HS-LS transition in the B1 structure is finished at ∼17 Å^3 only. Our calculations are in agreement with the quantitative analysis of x-ray emission spectroscopy data, which shows that MnSe keeps the high-spin state $S = 5/2$ until 15 GPa. Then in the range 15–30 GPa it exhibits an intermediate-spin state $S = 3/2$, and at a higher pressure, a low-spin state $S = 1/2$ is observed [4]. In Fig. 1(b), we present a schematic evolution of the Mn-3d crystal field splitting under pressure for both structures approximated from DMFT quantum impurity hybridization function and Green function occupations. Due to distortions in the $MnSe_6$ octahedra, the crystal field splitting of the B31 structure has trigonal-like form a_1–e_1–e_2. One should note that all orbitals of the B31 structure are nondegenerate, however a low energy pair of e_1 orbitals have almost the same energy, meanwhile high energy e_2 orbitals exhibit ∼5% energy difference between each other at AP and ∼10% at high pressure. Although no symmetry is present in the B31 structure, we use these notations for simplicity.

In order to investigate the nature of the spin transition in details, we carried out calculations of the electronic configurations distribution of the Mn-3d impurity within the DFT+DMFT method. Each electronic configuration can be described using $\hat{N}$ and $\hat{S}$ quantum numbers which commute with the local Hamiltonian of quantum impurity and can be straightforwardly calculated during quantum Monte Carlo hybridization-expansion impurity solver simulation. For the spin quantum number $\hat{S}$, its projection along the z axis was calculated. The obtained weights for relevant electronic configurations for each volume are presented in Fig. 2. Both the B1 and B31 structures have a very similar distribution of electronic configurations at each step of the HS-LS transition, with the only difference that the HS-LS in the B1 structure takes place at a smaller volume and the spin crossover range is wider. Therefore, we focus our discussion on the HS-LS transition of the B31 structure. At the lowest pressure, the high-spin state of the system consists of $d^5(S_z = 5/2)(80\%)$ and $d^6(2)(15\%)$ high-spin configurations, as expected for the Mn^{2+} ions. Under pressure, until 30 Å^3 no low-spin states is observed. Amidst the HS-LS transition, the intermediate-spin state configurations $d^5(3/2)(10\%)$, $d^6(1)(21\%)$, and $d^7(3/2)(10\%)$ dominate the spin state of the system at this volume [$d^7(3/2)$ is generally a high-spin configuration, but here it has dynamics of intermediate-spin configurations, thus we consider it such]. Further at smaller volumes the high-spin configurations vanish, the low-spin configurations, i.e., $d^6(0)(12\%)$, $d^5(1/2)(7\%)$, $d^7(1/2)(30\%)$, and $d^8(0)(10\%)$, become dominant and reach saturation, while the intermediate-spin configurations decrease in weight and become about 33% of the spin state of the system. The high amount of the intermediate spin configurations observed in our calculations agrees with the suggestion that MnSe exhibits the intermediate-spin state $S = 3/2$ at intermediate pressures [4]. The observed difference in the spin-transition pressure between the B1 and B31 structures comes down to the difference in total occupation number for both structures at the same volume: At AP volume the

difference is quite small (about 0.02 electrons), but at lower volumes the difference grows. For example, at $V = 24\,\text{Å}^3$ the Mn-3d states of the B31 structure have ∼0.25 electrons more. Higher occupation number with increasing pressure drives the spin transition at a faster rate, thus realizing a state with the lower energy at the same volume than would be possible with the B1 structure. Increased content of configurations with high occupation number in both structures (occupancy of quantum impurity under pressure grows on ∼1.5 electrons) is due to the increased strength of hybridization under compression.

The bath-impurity hybridization is an additional mechanism affecting the spin state of the system, as well as classical interplay of crystal field splitting and Hund energy. The calculated weights of the individual electronic configurations indicate that the hybridization is the cause of formation of the intermediate-spin configurations at all volumes. Derived from the calculated weights example scenarios of possible bath-impurity hybridization events leading to formation of the intermediate-spin configurations are presented in Fig. 2(b). Our calculations show that the most probable state of the Mn-3d shell is the HS $d^5(5/2)$ and the weight of the intermediate-spin $d^5(3/2)$ and $d^7(3/2)$ configurations is only a few percents at ambient pressure. The high hybridization strength of the high-energy e_g orbitals (we use orbital notation for the B1 structure here for simplicity) with Se-4p orbitals, and a weaker crystal field splitting at low pressure causes the bath-impurity hybridization events to occupy the e_g orbitals instead of t_{2g}: The $d^6(2)$ high-spin configuration is formed by adding hybridized e_g electron to the base $d^5(5/2)$ configuration; further bath-e_g hybridization forms the $d^5(3/2)$ and $d^7(3/2)$ configurations. Upon increased pressure, the e_g orbitals do not remain exclusive for hybridization events anymore, due to the increase in crystal field splitting. At high pressure, in the low-spin state the $d^5(3/2)$ and $d^6(0)$ configurations become more probable for formation for the intermediate-spin configurations via bath-e_g hybridization. However, as crystal field splitting under compression becomes large enough to trigger the change of a spin state, consequently, the ratio of intermediate-spin to low-spin configuration decreases. Similarly, the increase of hybridization strength under pressure keeps the intermediate-spin configurations from vanishing.

The distorted Mn environment in the B31 structure, which favors low-spin ordering, seems to be one of the main reasons for the experimentally observed structural phase transition. To investigate the mechanism of the structural transition, we calculate the DFT+DMFT total energy of both structures for a wide range of cell volumes. The obtained values of the DFT+DMFT total energy are presented in Fig. 3. The total energy curves of both structures exhibit two distinct low-pressure HS and high-pressure LS regimes with an obvious anomaly at the intermediate volumes, which corresponds to the rise of an intermediate-spin regime during the HS-LS crossover. For the HS and LS regimes of each structure, we performed a fit with the equation of state. Fitting the total energy of the low-pressure HS regime of the B1 structure with the equation of state we obtain parameters $V_0 = 40.25\,\text{Å}^3$ and $B_0 = 64.40\,\text{GPa}$, which are in good agreement with the experimental values $V_0 \approx 40\,\text{Å}^3$ and $B_0 = 68\,\text{GPa}$; note that DFT gave a $\sim 10\,\text{Å}^3$ smaller V_0 value. Incidentally, the low-pressure HS regime

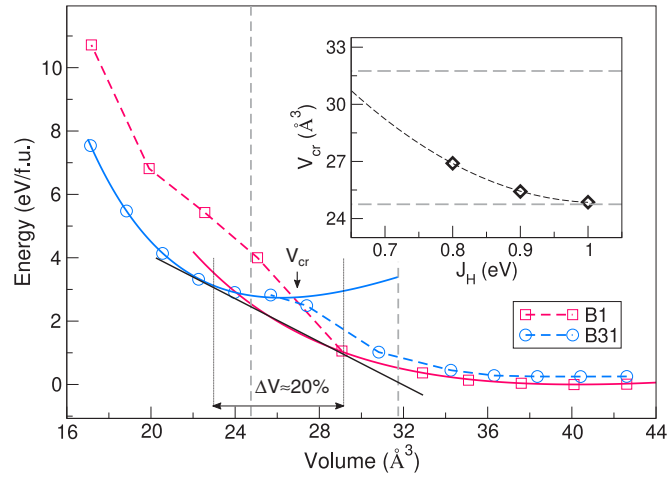

FIG. 3. The DFT+DMFT results for the total energy of MnSe as a function of volume for the cubic B1 and MnP-type B31 structures and the calculated Maxwell construction estimate of a cell volume collapse. The experimental phase transition cell volume range is shown by vertical dashed lines. Inset: structural phase transition volume V_{cr} versus the value of Hund interaction parameter J_H.

of the B31 structure almost exactly reproduces behavior of the B1 structure at low pressure, with the parameters of fit $V_0 = 39.89\,\text{Å}^3$ and $B_0 = 64.99\,\text{GPa}$ but has 0.53 eV higher total energy than the respective regime of the cubic structure, to the opposite of what is seen in DFT calculations. With increased pressure, after intermediate anomalous region, we observe the high-pressure LS regime of the B31 structure with the parameters of equation of state $V_0 = 26.21\,\text{Å}^3$ and $B_0 = 249.27\,\text{GPa}$. The bulk modulus of the B31 structure calculated from DFT+DMFT agrees with $B_0 = 218\,\text{GPa}$ reported by Wang *et al.* [4]. At the same time there exists inconsistency in the reported values for MnS, which the work reports to be $B_0 = 72$ and $B_0 = 80\,\text{GPa}$ for low- and high-pressure phases, respectively, indicating only small decrease in compressibility, meanwhile earlier work by Xiao *et al.* [3] reports respective values to be $B_0 = 60$ and $B_0 = 380\,\text{GPa}$, which are indicative of much larger increase in density after a volume collapse.

Our DFT+DMFT total energy shows that the high-pressure B31 structure becomes energetically profitable during the HS-LS transition in the anomalous region of both structures at volume of 27 Å^3. The total energy difference between the regimes of both structures, which is about 0.53 eV in the HS state, becomes −2.5 eV in the LS state and results in the structural phase transition. Crystal field splitting of Mn d-shell and hence more complicated picture of orbital energies arisen from distortion of $MnSe_6$ octahedron in the B31 structure is probably responsible for its higher total energy in the HS regime at low pressure and also makes the B31 structure more preferable at higher pressures in the LS state. Note that the decrease of V_0 due to the DMFT corrections of the high-pressure LS regime of the B31 structure is only $\sim 1\,\text{Å}^3$. To provide an estimate of magnitude of volume collapse we used the Maxwell construction procedure and obtained the difference of volumes to be 20%; the resulting volume range lies about $\sim 2\,\text{Å}^3$ lower than the one observed experimentally.

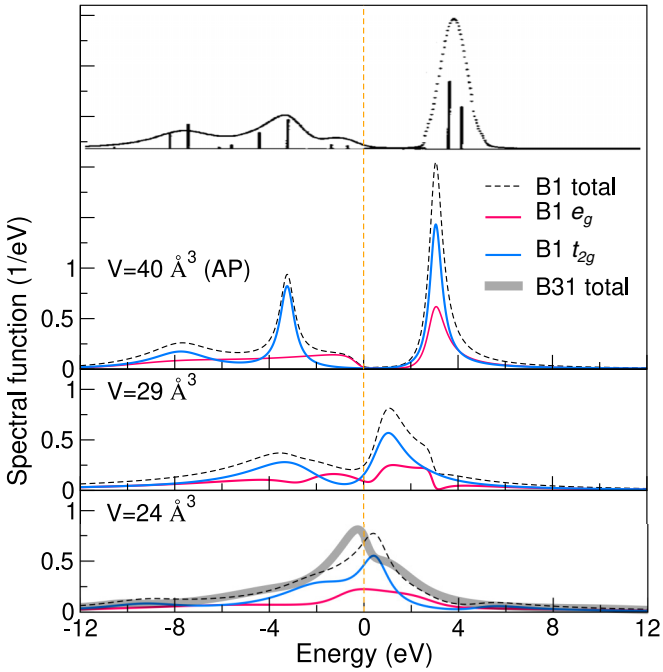

FIG. 4. Calculated within the DFT+DMFT method Mn-3*d* spectral functions at 1000 K of the manganese selenide MnSe at several volumes. The photoemission spectroscopy derived Mn-3*d* DOS from Ref. [19] is shown at the top.

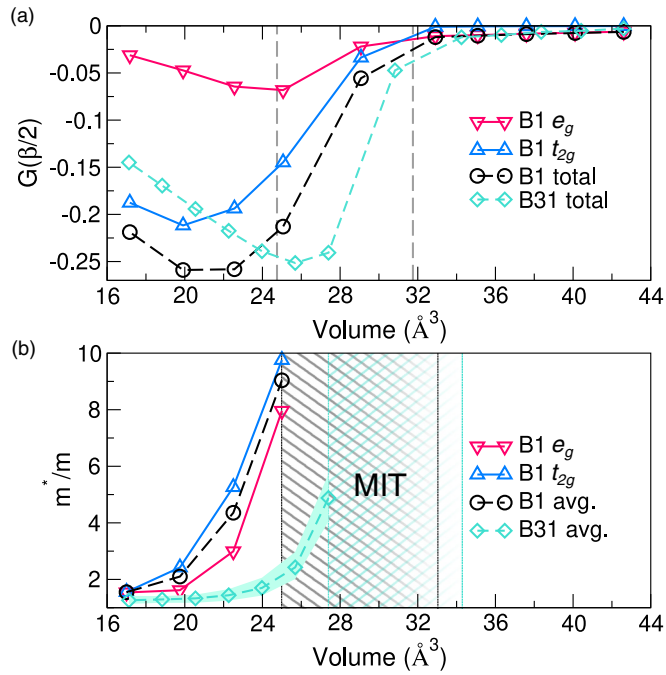

FIG. 5. (a) The DFT+DMFT Mn-3*d* imaginary time Green function at $\tau = \beta/2$ versus volume for the cubic B1 and MnP-type B31 structures. (b) Quasiparticle mass enhancement of Mn-3*d* orbitals for the B1 and B31 structures. Due to lack of degeneracy in the B31 structure the filled region shows extrema at each respective volume. The divergent region corresponding to the metal-insulator transition is marked by a respective rectangle for each structure.

To gain further insight into nature of the structural transition driven by the HS-LS transition, we repeated our calculations with enhanced values of Hund exchange parameter J_H of 0.9 eV and 1.0 eV. The obtained values of structural transition cell volume V_{cr} are presented in Fig. 3 (inset). As one would expect, we observed an increase of the critical pressure for the HS-LS transition and an increase of the spin crossover pressure range due to increased spin exchange energy for the higher J_H values. Consequently, the increase in the HS-LS transition pressure increases pressure required for the structural transition. If $J_H = 0.8$ eV the transition pressure is pretty close to the experimentally observed volume collapse conditions, albeit slightly lower. Higher J_H shifts the anomaly outside of expected volume range. The observed V_{cr} dependence from J_H parameter affirms $J_H = 0.8$ eV (or 0.86 eV from other works) to be preferable value. One would also have to consider the fact that density-density parametrization of the Coulomb interaction matrix used in this work is known to overestimate magnetic transitions. Further investigations with fully rotation-invariant form of the Coulomb interaction matrix are required.

In Fig. 4(a), we present the Mn-3*d* spectral functions of MnSe obtained in the DFT+DMFT calculations at AP, at the beginning of the HS-LS transition, and after the transition. In our calculations, at ambient pressure MnSe is an insulator with the gap of 2.0–2.1 eV, in good agreement with experiment; spectral features in the calculated DFT+DMFT spectral functions (peaks at ~ -7.7, -3.2, -1.0, 3.0 eV) reproduce spectral functions derived from PES and IPES measurements [19] (Fig. 4, at the top). The shape of MnSe spectral function resembles one of MnO which is considered as Mott insulator [7]. However, the detailed analysis of partial DOSes reveals that MnSe is closer to charge-transfer insulator or is in between both scenarios.

In Fig. 5(a), we present evolution of imaginary time Green functions at $\tau = \beta/2$ versus cell volume, which corresponds to the spectral weight at the Fermi level. Our results show that $G(\beta/2)$ are close to zero up to 33 Å^3, which is indicative of an insulating character. With increasing pressure, the value of $G(\beta/2)$ increases. This happens at the same volume when the value of the local magnetic moment begins to drop drastically, thus the metal-insulator transition. The $G(\beta/2)$ behavior for both structures correlates with the HS-LS transition, implying metal-insulator to be crystal field driven in similarity with MnO [7]. Individual curves of $G(\beta/2)$ for the t_{2g} and e_g orbitals of the B1 structure indicate no noticeable orbital selectivity during the insulator-metal transition. Our results are in agreement with electrical resistance measurements, where the metallization is reported to be accompanied by the structural transition [4]. The obtained $G(\beta/2)$ results agree with a calculated quasiparticle weight enhancement $m^*/m = 1 - \partial Im\,\Sigma(z)/\partial z|_{z=0}$, which can be used to estimate the correlation strength and is presented in Fig. 5(b). At the high pressure in the metallic phase, m^*/m converges to constant 1.3–1.5 for all orbitals of both structures which indicates moderate correlation strength. Upon cell expansion, following the dynamics of $G(\beta/2)$, the mass enhancement and consequently correlation strength in the metallic phase increases almost tenfold and then m^*/m diverges in the metal-insulator transition pressure region since self-energy loses its Fermi-liquid behavior.

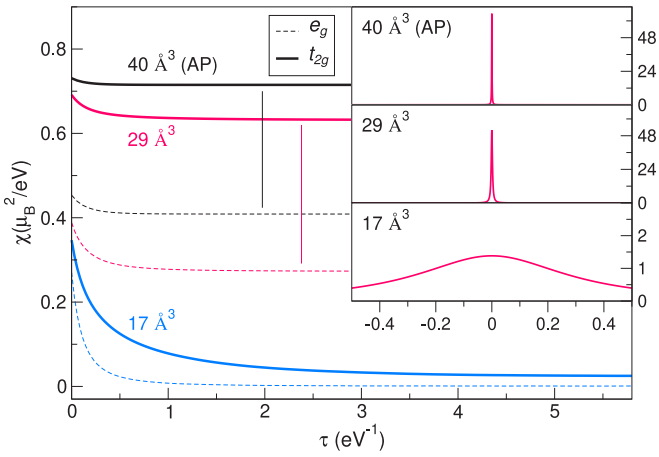

FIG. 6. The DFT+DMFT imaginary time and real frequency (inset) local spin susceptibility of Mn-3d t_{2g} and e_g orbitals for the cubic B1 structure at several volumes.

In Fig. 6, we show local spin susceptibility calculated within DFT+DMFT on imaginary time $\chi(\tau) = \langle \hat{m}_z(\tau)\hat{m}_z(0)\rangle$ and real frequency $\mathbb{R}\mathrm{e}\{\chi(\omega)\}$ at several volumes for the B1 structure. Our results show strong localization of the Mn-3d electrons at ambient pressure and up to the HS-LS transition. However, an increase in degree of delocalization is observed at pressure. Employing deductions of Igoshev *et al.* [42], we can estimate the degree of delocalization from a damping of the local moments δ (half width of $\chi(\omega)$ at half height) compared to $\pi T = 0.27$ eV. At AP and at onset of the phase transition ($V = 29$ Å^3), we obtain $\delta = 0.625$ meV and $\delta = 2.5$ meV, respectively, which indeed indicate strong localization, and only after the phase transition at $V = 17$ Å^3 we obtain comparative to πT value of the damping parameter $\delta = 0.32$ eV. The criteria for the itinerant regime $\delta \gtrsim \pi T$ is met after accomplishing the phase transition, thus we can conclude that during the HS-LS transition the Mn-3d electrons are still localized.

IV. CONCLUSIONS

In conclusion, we studied the electronic properties, magnetic state, and structural stability of the manganese selenide MnSe using the DFT+DMFT method. We computed the electronic structure and structural stability of the NaCl-type B1 and MnP-type B31 structures of MnSe under pressure in the paramagnetic state at temperature of $T = 1000$ K. Upon compression MnSe exhibits a high-spin to low-spin transition of Mn^{2+} ions which is accompanied by a structural B1 $\rightarrow$ B31 transition with a cell-volume collapse of $\sim$20%, in agreement with experimental data. Our results demonstrate an intermediate-spin $S = 3/2$ state in the anomalous pressure region of the transition.

Our results for the spectral properties show that at ambient pressure MnSe is an insulator with the gap of 2.0 eV. In agreement with experiment, the spin transition is accompanied by an insulator-to-metal transition with no orbital selectivity in the transition character. The calculated local spin susceptibility suggests that the Mn-3d electrons are well localized throughout the transition.

ACKNOWLEDGMENT

The research was supported by the Russian Science Foundation (Project No. 14-22-00004).

[1] A. Chatterjee, A. K. Singh, and A. Jayaraman, Phys. Rev. B **6**, 2285 (1972).
[2] S. A. J. Kimber, A. Salamat, S. R. Evans, H. O. Jeschke, K. Muthukumar, M. Tomić, F. Salvat-Pujol, R. Valentí, M. V. Kaisheva, I. Zizak, and T. Chatterji, Proc. Natl. Acad. Sci. USA **111**, 5106 (2014).
[3] G. Xiao, X. Yang, X. Zhang, K. Wang, X. Huang, Z. Ding, Y. Ma, G. Zou, and B. Zou, J. Am. Chem. Soc. **137**, 10297 (2015).
[4] Y. Wang, L. Bai, T. Wen, L. Yang, H. Gou, Y. Xiao, P. Chow, M. Pravica, W. Yang, and Y. Zhao, Angew. Chem. Int. Ed. **55**, 10350 (2016).
[5] K. Held, I. A. Nekrasov, G. Keller, V. Eyert, N. Blümer, A. K. McMahan, R. T. Scalettar, T. Pruschke, V. I. Anisimov, and D. Vollhardt, phys. stat. sol. (b) **243**, 2599 (2006).
[6] J. Kuneš, I. Leonov, P. Augustinský, V. Křápek, M. Kollar, and D. Vollhardt, Eur. Phys. J. ST **226**, 2641 (2017).
[7] J. Kuneš, A. V. Lukoyanov, V. I. Anisimov, R. T. Scalettar, and W. E. Pickett, Nat. Mater. **7**, 198 (2008).
[8] I. Leonov, A. V. Ponomareva, R. Nazarov, and I. A. Abrikosov, Phys. Rev. B **96**, 075136 (2017).
[9] A. O. Shorikov, Z. V. Pchelkina, V. I. Anisimov, S. L. Skornyakov, and M. A. Korotin, Phys. Rev. B **82**, 195101 (2010).
[10] A. A. Dyachenko, A. O. Shorikov, and V. I. Anisimov, JETP Lett. **106**, 317 (2017).
[11] A. O. Shorikov, A. V. Lukoyanov, V. I. Anisimov, and S. Y. Savrasov, Phys. Rev. B **92**, 035125 (2015).
[12] V. I. Anisimov and A. V. Lukoyanov, Acta Crystallogr., Sect. C **70**, 137 (2014).
[13] J.-F. Lin and T. Tsuchiya, Phys. Earth Planet. Inter. **170**, 248 (2008).
[14] J. Allen, G. Lucovsky, and J. Mikkelsen, Solid State Commun. **24**, 367 (1977).
[15] P. Klosowski, T. M. Giebultowicz, J. J. Rhyne, N. Samarth, H. Luo, and J. K. Furdyna, J. Appl. Phys. **69**, 6109 (1991).
[16] T. Ito, K. Ito, and M. Oka, Jpn. J. Appl. Phys. **17**, 371 (1978).
[17] R. J. Pollard, V. H. McCann, and J. B. Ward, J. Phys. C: Solid State Phys. **16**, 345 (1983).
[18] K. K. Kelley, J. Amer. Chem. Soc. **61**, 1217 (1939).
[19] H. Sato, T. Mihara, A. Furuta, M. Tamura, K. Mimura, N. Happo, M. Taniguchi, and Y. Ueda, Phys. Rev. B **56**, 7222 (1997).
[20] S. J. Youn, B. I. Min, and A. J. Freeman, phys. stat. sol. (b) **241**, 1411 (2004).
[21] V. I. Anisimov and O. Gunnarsson, Phys. Rev. B **43**, 7570 (1991).
[22] P. Amiri, S. J. Hashemifar, and H. Akbarzadeh, Phys. Rev. B **83**, 165424 (2011).
[23] A. A. Dyachenko, A. O. Shorikov, A. V. Lukoyanov, and V. I. Anisimov, JETP Lett. **96**, 56 (2012).

[24] J. Kuneš, D. M. Korotin, M. A. Korotin, V. I. Anisimov, and P. Werner, Phys. Rev. Lett. **102**, 146402 (2009).
[25] A. A. Dyachenko, A. O. Shorikov, A. V. Lukoyanov, and V. I. Anisimov, Phys. Rev. B **93**, 245121 (2016).
[26] A. V. Ushakov, A. O. Shorikov, V. I. Anisimov, N. V. Baranov, and S. V. Streltsov, Phys. Rev. B **95**, 205116 (2017).
[27] MN.PBE-SP-VAN.UPF, SE.PBE-VAN.UPF.
[28] P. Giannozzi, S. Baroni, N. Bonini, M. Calandra, R. Car, C. Cavazzoni, D. Ceresoli, G. L. Chiarotti, M. Cococcioni, I. Dabo, A. D. Corso, S. de Gironcoli, S. Fabris, G. Fratesi, R. Gebauer, U. Gerstmann, C. Gougoussis, A. Kokalj, M. Lazzeri, L. Martin-Samos, N. Marzari, F. Mauri, R. Mazzarello, S. Paolini, A. Pasquarello, L. Paulatto, C. Sbraccia, S. Scandolo, G. Sclauzero, A. P. Seitsonen, A. Smogunov, P. Umari, and R. M. Wentzcovitch, J. Phys.: Condens. Matter **21**, 395502 (2009).
[29] G. H. Wannier, Phys. Rev. **52**, 191 (1937).
[30] N. Marzari and D. Vanderbilt, Phys. Rev. B **56**, 12847 (1997).
[31] D. Korotin, A. V. Kozhevnikov, S. L. Skornyakov, I. Leonov, N. Binggeli, V. I. Anisimov, and G. Trimarchi, Eur. Phys. J. B **65**, 91 (2008).
[32] R. M. Wentzcovitch, J. L. Martins, and G. D. Price, Phys. Rev. Lett. **70**, 3947 (1993).
[33] http://www.amulet-code.org.
[34] P. Werner and A. J. Millis, Phys. Rev. B **74**, 155107 (2006).
[35] A. Albuquerque, F. Alet, P. Corboz, P. Dayal, A. Feiguin, S. Fuchs, L. Gamper, E. Gull, S. Gürtler, A. Honecker, R. Igarashi, M. Körner, A. Kozhevnikov, A. Läuchli, S. Manmana, M. Matsumoto, I. McCulloch, F. Michel, R. Noack, G. Pawłowski, L. Pollet, T. Pruschke, U. Schollwöck, S. Todo, S. Trebst, M. Troyer, P. Werner, and S. Wessel, J. Magn. Magn. Mater. **310**, 1187 (2007).
[36] K. S. D. Beach, R. J. Gooding, and F. Marsiglio, Phys. Rev. B **61**, 5147 (2000).
[37] B. Amadon, S. Biermann, A. Georges, and F. Aryasetiawan, Phys. Rev. Lett. **96**, 066402 (2006).
[38] P. Vinet, J. R. Smith, J. Ferrante, and J. H. Rose, Phys. Rev. B **35**, 1945 (1987).
[39] F. Birch, Phys. Rev. **71**, 809 (1947).
[40] H. Franzen and C. Sterner, J. Solid State Chem. **25**, 227 (1978).
[41] A. Mandale, S. Badrinarayanan, S. Date, and A. Sinha, J. Electron Spectrosc. Relat. Phenom. **33**, 61 (1984).
[42] P. A. Igoshev, A. V. Efremov, A. I. Poteryaev, A. A. Katanin, and V. I. Anisimov, Phys. Rev. B **88**, 155120 (2013).